Mesoscopic theory of wavefront shaping to focus waves deep inside disordered media

Bart A. van Tiggelen [*]
Université Grenoble Alpes, Centre National de la Recherche Scientifique (CNRS), Laboratoire de Physique et de Modélisation des Milieux Condensés (LPMMC), 38000 Grenoble, France

Ad Lagendijk
Complex Photonic Systems (COPS), MESA+ Institute for Nanotechnology, University of Twente, P.O. Box 217, 7500 AE Enschede, The Netherlands

Willem L. Vos [†]
Complex Photonic Systems (COPS), MESA+ Institute for Nanotechnology, University of Twente, P.O. Box 217, 7500 AE Enschede, The Netherlands and Université Grenoble Alpes, Centre National de la Recherche Scientifique (CNRS), Laboratoire de Physique et Modélisation des Milieux Condensés (LPMMC), 38000 Grenoble, France

(Received 14 October 2024; revised 11 February 2025; accepted 17 March 2025; published 5 May 2025)

We describe the theory of focusing waves to a predefined focal point deep inside a disordered three-dimensional (3D) opaque medium by the shaping of N different field sources outside the medium, also known as wavefront shaping. Our study is motivated by recent experiments where wavefront shaping, mediated by the controlled interference of scattered waves, coexists with a classical diffusion picture where wave interference appears irrelevant. We derive the energy density of the wave field both near the focal point and anywhere else inside the medium, averaged over realizations after optimizing the focus. To this end, we conceive of a point source at the focal point inside that emits waves to an external detector array that—by time reversal—becomes a source array that emits the desired shaped fields like a spatial light modulator. In this picture, the average energy density including the focusing is described by the C_1, C_2, C_3, and even C_0 intensity correlations known from mesoscopic transport theory. We draw the remarkable conclusion that by averaging over optimized wavefronts of the array, associated with different realizations of the disorder, a background energy density is obtained that obeys a diffusion equation in which C_2 correlations create an energy source inside. Hence a classical property (diffusion) coexists with interference (C_2 correlations). We derive the peak and background energy density distributions for C_0, C_1, and C_2 correlations, including for a slab. We find that the relative enhancement of the energy density at the focal point is proportional to the angular opening of the array, which *de facto* replaces the role of the inverse dimensionless conductance $1/g$ as the universal parameter in the transmission statistics, and it generalizes the number of segments known from experiments. We exploit the concept of a source for "optimized background energy" inside the medium to compare several different energy density profiles proposed in the literature, which are associated with optimized transmission by a slab using wavefront shaping. We explain why the best matching models have the first diffusion mode dominating, as was found in earlier work. Our approach avoids random-matrix theory restricted to waveguide geometries, confirms the role non-Gaussian correlations in the wavefront shaping for focusing deep inside 3D random media, and highlights the notion of an energy source created in this process. Our results are relevant for applications where the internal energy density in opaque media is crucial, varying from white-light illumination, projection optics, semiconductor metrology, (bio)sensing, to photovoltaics.

DOI: 10.1103/PhysRevA.111.053507

I. INTRODUCTION

It is a remarkable feat in optics, microwaves, elastic waves, and acoustics that waves can be focused to predefined points inside disordered opaque media by the judicious manipulation of incident wavefronts [1–4], known as "wavefront shaping" (WFS) [5]. Wavefront shaping is efficient because multiple scattering is characterized by short-range correlations that can suppress statistical fluctuations. In wavefront shaping, one manipulates the phases and amplitudes of spatial or spectral elements of an incident wave packet to optimize, by interference, the focusing to a predefined point, or the total transmission, or even the delay time [2,6]. Recent wavefront shaping studies have demonstrated that even the energy density of the waves is enhanced inside three-dimensional (3D) media

[*]Contact author: Bart.Van-Tiggelen@lpmmc.cnrs.fr
[†]Contact author: w.l.vos@utwente.nl

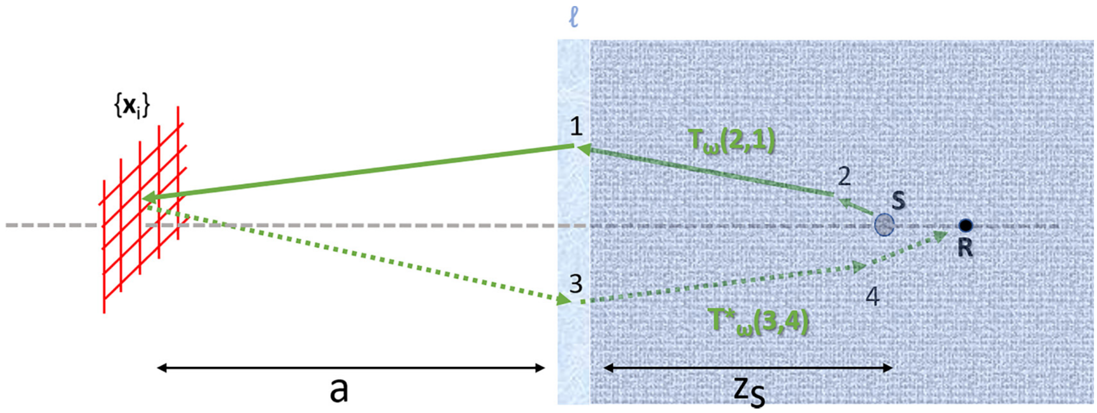

FIG. 1. Schematic of wavefront shaping to focus waves to a point S at a depth z_s inside a disordered 3D semi-infinite medium (half space) on the right. At the surface, the medium has a skin layer with a thickness of about one mean free path ℓ (blue, center). A wave packet from a virtual point source at S is sent to the detector array with N detectors at positions $\{\mathbf{x}_i\}$ at a large distance a in the far field of the medium, with $a \gg z_S$. Optimal shaping is established by time reversal of the entire wave packet that necessarily refocuses on a diffraction-limited spot $R \approx S$ with a background energy calculated in this work for all positions R. The path of the wave from source to array (solid arrows) is distinguished into three parts: (I) emission of energy by a virtual source at focus S to a nearby scatterer $\boldsymbol{r}_2$, (II) radiative transport towards position $\boldsymbol{r}_1$ in the skin layer with T-matrix $T_\omega(2,1) \equiv T_\omega(\boldsymbol{r}_2, \boldsymbol{r}_1)$, and (III) ballistic propagation from the skin layer towards the array. The time-reversed signal (dashed arrows) (I′) propagates to the skin layer (position 3), (II′) radiative transport from skin layer to point $\boldsymbol{r}_4$ in the medium with T-matrix $T^*_\omega(\boldsymbol{r}_3, \boldsymbol{r}_4)$, (III′) scattering from $\boldsymbol{r}_4$ to the receiving point R.

[7,8], in two-dimensional (2D) media [9,10], or in quasi-1D media [11]. Surprisingly, it was found that after optimizing a spot on the sample's back surface, the density profile inside the medium is dominated by the first eigenmode of the diffusion equation [12], as confirmed by Davy *et al.* [13] and Koirala *et al.* [14] for lower-dimensional systems. This feature is remarkable since WFS invokes wave interferences, whereas diffusion describes intensities, hence no interferences, yet no simple explanation has been given to date for this notion. To address this challenge, we analyze in this paper the WFS to focus an incident wave packet to a given point deep inside a 3D disordered medium. The present work addresses the focusing of waves in 3D random media, applies arguments developed for time reversal [15], and is intimately connected to the experimental approach pioneered by Vellekoop and Mosk [16] to describe WFS by a spatial light modulator (SLM) to optimize transmission in the far field. The focusing of a time-reversed wave packet is stable against statistical fluctuations provided its frequency bandwidth $\Delta\omega$ is larger than the typical decorrelation frequency, which is small deep inside diffusive media [17]. This notion was recently confirmed by the focusing of broadband light in a disordered 2D medium [18]. The analogy of focusing by time reversal and WFS is helpful for two reasons. First, it establishes the link between long-range non-Gaussian C_2 fluctuations in transmission [19,20] and focusing *outside* the random medium [16]. Second, it provides simple expressions for the peak-to-background enhancement [10,18,21] near the focus inside the medium, even for a 3D slab geometry where random-matrix theory does not apply, and where our innovation is that we derive our theory for sources *inside*. In particular, the analogy between time reversal and wavefront shaping reveals that long-range correlations create a genuine source near the focal point, in addition to the designed constructive interference that induces the focus, governed by short-range spatial fluctuations. This picture reveals the coexistence of diffuse waves and wave interference, as in time-reversal physics [15,17]. Although the focused energy is governed by the local density of states (LDOS), the statistical fluctuations of the LDOS, known as C_0 speckle [22–25], are found to be small.

Figure 1 shows and describes the setup for a disordered half-space. We use a mesoscopic theory with a statistical approach to deal with wave fluctuations. This approach does not reveal information on individual realizations, such as the specific realization that optimizes some observable. Nevertheless, given a specific realization of the disorder, the wavefront to be emitted by an array of sources designed to optimally focus to a point S inside the random medium can be obtained by first sending a wave packet from a virtual source at S, and time-reversing the received signal at the array. The array now plays the role of the spatial light modulator introduced by Refs. [1,16,26] to focus outside the medium, and by Ref. [10] to focus inside the medium. This means that the signal radiated by the array is highly correlated with wave propagation in the random medium, unlike the standard situation in radiative transfer [27–29].

We consider a near-monochromatic wave packet and an array with angular opening Ω_A. This array sends plane waves with propagation directions inside the solid angle Ω_A when the phases emitted by the different elements $\{\mathbf{x}_i\}$ vary linearly. When they are manipulated otherwise, many complicated wavefronts can be achieved. Here we want to employ WFS to focus to a point S in the medium. The time-reversal method implicitly generates an ideal candidate, though not necessarily unique. In addition, scattering from disorder generates a background energy density of the wave field that varies with the position of point R in Fig. 1. Intuitively, we may expect the focal point S to become a secondary source of energy for diffuse waves in the random medium and contribute to this background energy. We will analyze different correlations of type C_0 (fluctuations in the local density of states), C_1 (Gaussian speckle intensity), and C_2 (total transmission fluctuations) known in mesoscopic wave physics, and we will show that C_2 makes a dominant contribution to the energy density of the waves away from focal spot, and also generates this expected source.

II. TIME REVERSAL TO OPTIMIZE WAVEFRONTS

Because long-range diffusion is taken to be isotropic, the typical diffuse halo created at the sample surface in Fig. 1 by a virtual source at depth z_S has a radius z_S. We will also assume that the distance a of the array satisfies $a \gg z_S$. In that case, waves arriving at points 1 and 3 in Fig. 1 still have approximate normal incidence. The average propagation from array element $\mathbf{r_i} = \mathbf{a} + \mathbf{x_i}$ to the point $\mathbf{r_1}$ in the skin layer is described by the Green function

$$G(\mathbf{r}_i, \mathbf{r}_1) = -\frac{1}{4\pi|\mathbf{r}_i - \mathbf{r}_1|}e^{ik|\mathbf{r}_i-\mathbf{r}_1|}e^{-z_1/(2\ell\cos\theta_i)}$$
$$\approx -\frac{1}{4\pi a}e^{ika}e^{-ik\boldsymbol{\rho}_1\cdot\mathbf{x}_i/a}e^{-z_1/2\ell}, \quad (1)$$

where θ_i is the angle between $\mathbf{r_i}$ and the normal to the slab that is assumed to be small. For a point $\mathbf{r_2}$ near S or deep in the medium, we adopt the bulk expression for average wave propagation,

$$G(\mathbf{r}_S, \mathbf{r}_2) = -\frac{1}{4\pi|\mathbf{r}_S - \mathbf{r}_2|}e^{i(k+i/2\ell)|\mathbf{r}_S-\mathbf{r}_2|}, \quad (2)$$

which restricts the position of point $\mathbf{r_2}$ to be within one mean free path ℓ from S, and the same holds for a point $\mathbf{r_4}$ near the point of measurement R. In Fig. 1, we have drawn R on the axis fixed by virtual source S and array center, but in the next section we allow any transverse translation over a distance ρ, which will be important to find the background energy.

Let us briefly recall the process of time reversal, adapted to the present simplified context. For scalar waves, time reversal reduces to complex conjugation. When the virtual source at S with complex and band-limited Fourier-amplitude $v_S(\omega)$ starts releasing its energy at $t = 0$, the field is registered outside the medium on the array between times $0 < t < T$, sent back (time-reversed) immediately with complex amplitude $v_T(\omega)$ assumed independent on array element i, and measured at point R at time $\tau > T$. We assume that the signal has a spectral bandwidth $\Delta\omega$ small enough to be considered quasi-monochromatic but that $T \gg 2\pi/B$. The field sent back into the medium and arriving at R is then given by [15,30]

$$\Phi(R, \tau + 2T) = \int_{-\infty}^{\infty}\frac{d\omega}{2\pi}e^{-i\omega\tau}v_S(\omega)G(\mathbf{r}_S, \mathbf{r}_i, \omega + i0)$$
$$\times\, v_T(\omega)G(\mathbf{r}_i, \mathbf{r}, \omega + i0)^*. \quad (3)$$

From previous work, we know that this signal typically contains an arrival at $\tau < 0$ and—by reciprocity—one at $\tau > 0$ associated with waves traveling from S to R and *vice versa*. In the frequency domain, we can split this propagation up into different parts as shown in Fig. 1,

$$\Phi(\boldsymbol{r}, \boldsymbol{r}_S, \omega) = \chi\sum_{i=1}^{N}\int d\boldsymbol{r}_1 d\boldsymbol{r}_2 d\boldsymbol{r}_3 d\boldsymbol{r}_4 G(\mathbf{r}_S, \mathbf{r}_2)T(\mathbf{r}_2, \mathbf{r}_1)$$
$$\times\, G(\mathbf{r}_1, \mathbf{r}_i)G^*(\mathbf{r}_i, \mathbf{r}_3)T^*(\mathbf{r}_3, \mathbf{r}_4)G^*(\mathbf{r}_4, \mathbf{r}), \quad (4)$$

with all factors taken at equal frequency, therefore the frequency label is omitted from now on. We have summarized the "virtual" source v_S and any possible loss or gain factor v_T in the array by a complex number χ. Hereafter, we shall put $\Phi_0 = \chi/(4\pi a)^2$ as the reference amplitude for the wavefront sent by the array to the sample surface, with the same unit as the field Φ. The quality of focusing is determined by (i) the size of the focal spot around S, and (ii) the ratio of peak value in energy at S and surrounding the "average background." As mentioned earlier, we expect this background to contain a component associated with a real source at S. In time-reversal experiments, a sufficiently large bandwidth (that is, larger than the Thouless frequency proportional to D/z_s^2 that separates uncorrelated frequencies) guarantees self-averaging and stability of the process. In this work, this is ensured by the sufficiently large opening of the array.

The wave field $\Phi(\mathbf{r}, \omega)$ derived in Eq. (4) from time reversal contains the two scattering matrices $T(\mathbf{r}_2, \mathbf{r}_1)$ and $T^*(\mathbf{r}_3, \mathbf{r}_4)$. We obtain its statistical average from standard transport theory [20]. In the diffusion approximation, we find for the scattering matrices that

$$\langle T(\mathbf{r}_2, \mathbf{r}_1)T^*(\mathbf{r}_3, \mathbf{r}_4)\rangle$$
$$= \mathcal{L}(\mathbf{r}_1, \mathbf{r}_2)[\delta(\boldsymbol{r}_1, \boldsymbol{r}_3)\delta(\boldsymbol{r}_2, \boldsymbol{r}_4) + \delta(\boldsymbol{r}_1, \boldsymbol{r}_4)\delta(\boldsymbol{r}_2, \boldsymbol{r}_3)] \quad (5)$$

with the propagator $\mathcal{L}$ obeying the stationary diffusion equation

$$-\frac{1}{3}\ell^*\nabla^2\mathcal{L}(\boldsymbol{r}, \boldsymbol{r}') = \frac{4\pi}{\ell^2}\delta(\boldsymbol{r}, \boldsymbol{r}'), \quad (6)$$

where ℓ^* is the transport mean free path. To simplify, we assume $\ell^* = \ell$ in the rest of this paper. The two terms in Eq. (5) are imposed by reciprocity, but the second "Coherent Backscattering" term only contributes when point 1 is close to point 2. Hence the second term is excluded because $\mathbf{r}_1$ is located in the skin layer, whereas $\mathbf{r}_2$ is close to S deep in the bulk. It immediately follows that

$$\Phi(\boldsymbol{r}, \boldsymbol{r}_S) = \Phi_0 N\frac{\ell}{4\pi}P(\mathbf{r}_S, \mathbf{r}_R)\int_0^{\infty}dz_1 e^{-z_1/\ell}\mathcal{L}(z_S, z_1, \mathbf{q} = \mathbf{0}).$$

Here N is the number of elements in the array that all contribute equally and coherently, and $\mathbf{q}$ is the transverse Fourier component; $\mathbf{q} = \mathbf{0}$ appears because the effective area $\sim z_S^2$ illuminated by the source is much smaller than the area $\sim a^2$ available. We also used that

$$\int_2 G(\mathbf{r}_S, \mathbf{r}_2)G^*(\mathbf{r}_2, \mathbf{r}) = \frac{\ell}{4\pi}\frac{-\mathrm{Im}\,G(\mathbf{r}_S, \mathbf{r})}{-\mathrm{Im}\,G(0)} \equiv \frac{\ell}{4\pi}P(\mathbf{r}_S, \mathbf{r}), \quad (7)$$

which describes a diffraction-limited peak near S oscillating at the scale of the wavelength and decaying exponentially with the mean free path ℓ.

If we impose the usual radiative boundary condition $\mathcal{L}(-z_0, z) = 0$ for all z, with $z_0 \approx \frac{2}{3}\ell$, it follows from the diffusion equation that $\mathcal{L}(z, z', \mathbf{q} = \mathbf{0}) = (12\pi/\ell^3)[z_0 + \min(z, z')]$. To avoid messy formulas, especially later on, we will approximate the integrals $\int dz\exp(-z/\ell)f(z) \approx \ell f(0)$ for any smooth function $f(z)$. Then, for $z > 0$, the focused amplitude becomes

$$\langle \Phi(\boldsymbol{r}, \boldsymbol{r}_S) \rangle = \Phi_0 \times N \times \frac{3z_0}{\ell} P(\mathbf{r}_S, \mathbf{r}). \tag{8}$$

It is independent of the depth of the focal point S, and it vanishes when R is located beyond one mean free path of the point S. The focal amplitude is proportional to the number of array elements N. Hence the focal energy density scales as N^2. In the next section, we will show that the background scales as N, so that the focal enhancement scales as N, as is generally expected in wavefront-shaping experiments; see, e.g., Refs. [1,2,5,7,26].

III. SPATIAL CORRELATIONS FOR FOCUS AND BACKGROUND

The next step is to describe the energy density. We expect a peak energy around the focus S and a diffuse background energy everywhere else that varies smoothly in space. The average energy density is proportional to $\langle |\Phi(\mathbf{r})|^2 \rangle$ and involves the average of four scattering matrices,

$$\langle T(\mathbf{r}_2, \mathbf{r}_1) T^*(\mathbf{r}_3, \mathbf{r}_4) T^*(\mathbf{r}_{2'}, \mathbf{r}_{1'}) T(\mathbf{r}_{3'}, \mathbf{r}_{4'}) \rangle. \tag{9}$$

We apply mesoscopic theory as reviewed by Berkovits and Feng and Van Rossum and Nieuwenhuizen [19,20] to find the required correlators. This theory was developed to calculate fluctuations in transmission, reflection, and conductance, and it expands in the so-called inverse dimensionless conductance $1/g$, which is known to be small in the diffuse regime. Given two scattering matrices and two complex conjugates, exactly three kinds of correlations are identified, written traditionally as C_1, C_2, and C_3, depending on the way they correlate incoming and outgoing channels (see Ref. [31] for a measurement of all long-range correlations). When we adapt this theory to WFS inside the diffuse medium, the different correlations will produce different contributions to focal spot and background energy densities. The small parameter in the expansion is no longer $1/g$ [32] but rather the angular opening of the array that also describes the ratio of peak-to-background energy. The C_2 correlation is known to correlate either all input or output channels and dominates for that reason the fluctuations of the total transmission into all outgoing channels of a fixed input channel. The quantity $C_{4,2} = \frac{2}{3}$ introduced by Vellekoop and Mosk [16] determines the maximum achievable transmission by WFS and is a manifestation of long-range C_2 correlations without which the C_1 approximation would give a much lower value $C_{4,2} \sim \ell/L$ proportional to the usual ensemble-averaged transmission. Here C_2 will be seen to produce an energy source *inside* the medium. The lengthy calculations of the C_3 correlations in WFS will be deferred to future work.

A. C_1 correlations

In the well-known C_1 approximation, we have Gaussian decoupling of the complex conjugates [20],

$$\begin{aligned}
&\langle T(\mathbf{r}_2, \mathbf{r}_1) T^*(\mathbf{r}_3, \mathbf{r}_4) T^*(\mathbf{r}_{2'}, \mathbf{r}_{1'}) T(\mathbf{r}_{3'}, \mathbf{r}_{4'}) \rangle \\
&\quad = \langle T(\mathbf{r}_2, \mathbf{r}_1) T^*(\mathbf{r}_3, \mathbf{r}_4) \rangle \langle T^*(\mathbf{r}_{2'}, \mathbf{r}_{1'}) T(\mathbf{r}_{3'}, \mathbf{r}_{4'}) \rangle \\
&\qquad + \langle T(\mathbf{r}_2, \mathbf{r}_1) T^*(\mathbf{r}_{2'}, \mathbf{r}_{1'}) \rangle \langle T^*(\mathbf{r}_3, \mathbf{r}_4) T(\mathbf{r}_{3'}, \mathbf{r}_{4'}) \rangle,
\end{aligned} \tag{10}$$

where the dashes refer to the positions in the path followed by the time-reversed path. In the mesoscopic theory for transmission, the first term is the diffuse intensity squared, and the second term the short-range intensity speckle. In the context of WFS, the first term refers to the focused peak energy density P (at $R \approx S$), and the second term refers to the diffuse energy density B of the background.

Given the average amplitude found in Eq. (8), the first term on the right-hand side of Eq. (10) is equal to

$$P_1(\mathbf{r}) = 9|\Phi_0|^2 N^2 P(\mathbf{r}_S, \mathbf{r})^2 \left(\frac{z_0}{\ell}\right)^2. \tag{11}$$

We note that the spot is not due to a local energy source; see Appendix B. In this steady-state picture, the focus is due to the designed constructive interference between incoming and outgoing waves at S that causes the energy to accumulate locally, similar to what happens in the focal spot after time reversal [33] or in coherent backscattering.

The second term in Eq. (10) generates a "diffuse" background energy B_1 that depends on R but without a distinct peak near S. This background suffers from dephasing among the phase factors $\exp(ik\boldsymbol{\rho}_i \cdot \boldsymbol{x}_i/a)$ in Eq. (1), leading to

$$B_1(z, \boldsymbol{\rho}) = |\Phi_0|^2 \frac{\ell^4}{(4\pi)^2} \sum_{ij} \mathcal{L}(0, z_S, \mathbf{q}_{ij}) \mathcal{L}(0, z, \mathbf{q}_{ij}) e^{i\mathbf{q}_{ij}\cdot\boldsymbol{\rho}} \tag{12}$$

with the transverse wave vector $\mathbf{q}_{ij} = [k(\mathbf{x}_i - \mathbf{x}_j)/a]$ governing interference between different array elements. For finite $\mathbf{q}$, the diffusion propagator takes the form

$$\mathcal{L}(z, z', \mathbf{q}) = \frac{12\pi}{\ell^3} \frac{e^{-q|z-z'|} - e^{-q(z+z'+2z_0)}}{2q}. \tag{13}$$

If the typical distance between array elements obeys $\Delta x < (\lambda/2\pi)a/z_s$, which holds if a/z_S is sufficiently large (see Fig. 1), the integrand of Eq. (12) hardly varies from one array element to another. Hence, the sum over j can be replaced by an integral that is independent on i since the propagator $\mathcal{L}(z_s, 0, q)$ decays rapidly with q for $z_S \gg \ell$. Let us introduce the total solid angle Ω_A subtended by the SLM array from the viewpoint of the sample

$$\Omega_A = N \frac{(\Delta x)^2}{a^2}. \tag{14}$$

Then we obtain $\sum_{ij} \to N \times (N/k^2\Omega_A) \int d^2\mathbf{q}$. For $\Omega_A \ll 2\pi$, the incidence for all array elements is nearly normal. For $z > 0$, the expression for the C_1-background energy B_1 reduces to

$$\begin{aligned}
B_1(z, \boldsymbol{\rho}) &= \frac{|\Phi_0|^2 N^2 \ell^4}{(4\pi)^2 k^2 \Omega_A} \int d^2\mathbf{q}\, \mathcal{L}(0, z_S, \boldsymbol{q}) \mathcal{L}(0, z, \boldsymbol{q}) e^{i\boldsymbol{q}\cdot\boldsymbol{\rho}} \\
&= 9|\Phi_0|^2 N^2 \frac{z_0^2}{\ell^2} \frac{2\pi}{k^2 \Omega_A} \frac{z + z_S + 2z_0}{[(z + z_S + 2z_0)^2 + \rho^2]^{3/2}}.
\end{aligned} \tag{15}$$

For S near the sample surface, this expression is proportional to the familiar emission of a diffuse point source created by a focus from outside [34]. For S deep in the medium, the energy density is roughly constant as long as $z, \rho < z_S$. The diffuse transverse halo has a typical surface that grows with depth according to

$$\langle \rho^2(z, z_S)\rangle_1 \equiv \frac{\int d^2\boldsymbol{\rho}\, B_1(z, \boldsymbol{\rho})}{B_1(z, \boldsymbol{\rho}=\mathbf{0})} = 2\pi(z + z_S + 2z_0)^2, \quad (16)$$

which is small compared to πa^2 at the surface ($z = 0$) when $a \gg z_S$, which justifies the assumption made just below Eq. (13). The quality of the focus is conveniently quantified by the enhancement defined as the ratio of the peak and the background energy P/B [8,26]. Near the location of S given by $S = (z_S, (\boldsymbol{\rho} = \mathbf{0}))$ (see Fig. 1), the enhancement is equal to

$$\frac{P_1(\mathbf{r} = \mathbf{r}_S)}{B_1(\mathbf{r} = \mathbf{r}_S)} \approx \frac{\Omega_A}{2\pi} \times [2k(z_S + z_0)]^2. \quad (17)$$

Equation (17) shows that in the C_1 approximation, the enhancement is proportional to the angular opening of the array (and hence to the number of array elements N), which is small, and to the square of the focal depth in units of the wavelength, which is large. The finite angular coverage suppresses the C_1 background and makes the focus prominent and stable against statistical fluctuation in the medium [17].

In Appendix A, we derive the major result that the background energy density B_1, despite being produced here by a time-reversal procedure, obeys the *diffusion equation* known for diffuse energy produced by normal incident radiation, in particular with the same diffusion constant D. The diffusion equation is also characterized by a source of energy proportional to $-\nabla^2 B_1$. From Eq. (15) we infer that the source power is proportional to $\mathcal{L}(0, z_s, \boldsymbol{\rho})\delta(z) \simeq \delta(z) \times z_S/(z_S^2 + \rho^2)^{3/2}$, that is, only at the sample's surface and with a finite transverse width equal to z_S. Because no other source exists in the medium, and since no flux is transmitted either, the power flux F_1 across any transverse surface is given by

$$F_1(z > 0) = \int d^2\boldsymbol{\rho} J(z, \boldsymbol{\rho}) = -D\partial_z \int d^2\boldsymbol{\rho} B_1(z, \boldsymbol{\rho}) = 0, \quad (18)$$

which thus vanishes. Nevertheless, for any $z > 0$ and for fixed $\boldsymbol{\rho}$, the current density itself does not vanish. Since the incident flux vanishes due to the radiative boundary condition $B_1(-z_0) = 0$, the totally reflected (average) flux is given by

$$F_1(z < 0) = -D \int d^2\boldsymbol{\rho}\, \partial_z B_1(z < 0, \boldsymbol{\rho}) = -\frac{9|\Phi_0|^2 N^2}{(k\ell)^2} \frac{(2\pi)^2 z_0^2}{\Omega_A} \times \frac{c_0}{2} \quad (19)$$

with $z_0 = 2\ell/3$ and $D = c_0\ell/3$. We need this outgoing flux later when we include C_2 to normalize the reflection coefficient.

B. C_2 correlation and internal source

In this section, we investigate the importance of C_2 correlations for the focusing of energy at point S and its surrounding energy density. We show that the small parameter in the expansion of correlations is the angular opening of the array $\Omega_A/2\pi$ illustrated in Fig. 1.

In the mesoscopic theory [20], intensity correlation functions achieve non-Gaussian terms because different paths exchange momentum by scattering from the same particle, as qualified by a so-called Hikami vertex [32]. The lowest-order contribution is obtained when this crossing happens only once. For correlations of the kind $\langle GG^*GG^*\rangle$ involving two paths and two complex-conjugated paths, only two diagrams can be identified, shown in Fig. 2. The diagram in Fig. 2 (left) is expected to contribute to the background because it is proportional to $\delta(\boldsymbol{r}_1, \boldsymbol{r}_3)\delta(\boldsymbol{r}_1', \boldsymbol{r}_3')\delta(\boldsymbol{r}_2, \boldsymbol{r}_2')\delta(\boldsymbol{r}_4\boldsymbol{r}_4')$. This links both end points $\mathbf{r}_4$ and $\mathbf{r}_{4'}$ to the point of observation R and does not decorrelate when R changes (recall Fig. 1). In addition, since the pairs ($\mathbf{r}_1$, $\mathbf{r}_3$) and ($\mathbf{r}_{1'}$, $\mathbf{r}_{3'}$) are linked, the diagram is also insensitive to phase differences between waves received and emitted by the array, as is the case for the peak energy in Eq. (11). On the other hand, the diagram in Fig. 2 (right) is proportional to $\delta(\boldsymbol{r}_2, \boldsymbol{r}_4)\delta(\boldsymbol{r}_2', \boldsymbol{r}_4')$ and only survives when R and S are separated by at most one mean free path and thus contributes to focusing. This is consistent with Ref. [16], where it leads to a maximal optimized transmission of 2/3. The decorrelation between different array elements makes it a factor $\Omega_A(kz_S)^2$ smaller than the C_2 diagram in Fig. 2 (right) and gives a negligible correction to the C_1 peak P_1. We estimate for the peak under the C_2 correlations that it is negligible compared to the peak under C_1 correlations: $P_2 \sim B_1(\boldsymbol{r}_S)/(k\ell)^2 \ll P_1$.

The C_2 diagram in Fig. 2 (left) is expressed mathematically as [20]

$$\langle T(\mathbf{r}_2, \mathbf{r}_1)T^*(\mathbf{r}_3, \mathbf{r}_4)T^*(\mathbf{r}_{2'}, \mathbf{r}_{1'})T(\mathbf{r}_{3'}, \mathbf{r}_{4'})\rangle_{C_2} = N_H \int d^3\mathbf{H} \left[\nabla_a \cdot \nabla_b + \nabla_c \cdot \nabla_d - \frac{1}{2}\sum_{i=abcd} \nabla_i^2\right]_{abcd=\mathbf{H}} \mathcal{L}(\mathbf{r}_1, \mathbf{r}_a)\mathcal{L}(\mathbf{r}_{1'}, \mathbf{r}_b) \times \mathcal{L}(\mathbf{r}_c, \mathbf{r}_2)\mathcal{L}(\mathbf{r}_d, \mathbf{r}_4)\delta(\boldsymbol{r}_2, \boldsymbol{r}_2')\delta(\boldsymbol{r}_4, \boldsymbol{r}_4')\delta(\boldsymbol{r}_1, \boldsymbol{r}_3)\delta(\boldsymbol{r}_1', \boldsymbol{r}_3'), \quad (20)$$

with $\nabla_a \equiv \partial/\partial \mathbf{r}_a$, $N_H = \ell^5/48\pi k^2$, and $\boldsymbol{H}$ is the location of the Hikami vertex in the medium. The diffuse kernel $\mathcal{L}$ was defined earlier in Eq. (6). With this, the background energy density $B_2(\boldsymbol{r})$ at position R for C_2 correlations is given by

$$B_2(\boldsymbol{r}, \boldsymbol{r}_S) = |\Phi_0|^2 N_H \int d\mathbf{r}_1 d\mathbf{r}_{1'} d\mathbf{r}_2 d\mathbf{r}_4 \int d^3\mathbf{r}_H \sum_{ij}^{N} |G(\mathbf{r}_2, \mathbf{r}_S)|^2 |G(\mathbf{r}_4, \mathbf{r})|^2 |G(\mathbf{r}_1, \mathbf{r}_i)|^2 |G(\mathbf{r}_{1'}, \mathbf{r}_j)|^2 \Big[\nabla_{\mathbf{H}}\mathcal{L}(\mathbf{r}_1, \mathbf{r}_H) \cdot \nabla_H \mathcal{L}(\mathbf{r}_{1'}, \mathbf{r}_H)\mathcal{L}(\mathbf{r}_H, \mathbf{r}_2) \times \mathcal{L}(\mathbf{r}_H, \mathbf{r}_4) + \mathcal{L}(\mathbf{r}_1, \mathbf{r}_H)\mathcal{L}(\mathbf{r}_{1'}, \mathbf{r}_H)\nabla_H \mathcal{L}(\mathbf{r}_H, \mathbf{r}_2) \cdot \nabla_H \mathcal{L}(\mathbf{r}_H, \mathbf{r}_4) - \frac{1}{2}\sum_{i=abcd} \nabla_i^2 \mathcal{L}(\mathbf{r}_1, \mathbf{r}_a)\mathcal{L}(\mathbf{r}_{1'}, \mathbf{r}_b)\mathcal{L}(\mathbf{r}_c, \mathbf{r}_2)\mathcal{L}(\mathbf{r}_d, \mathbf{r}_4)\Big]_{abcd=\mathbf{H}}. \quad (21)$$

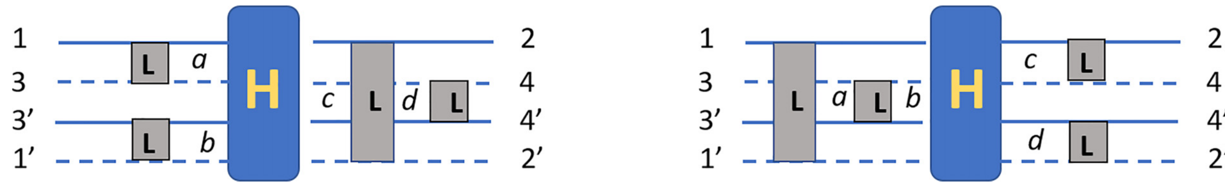

FIG. 2. Hikami diagrams for C_2 correlations in the average $\langle T(\boldsymbol{r}_2,\boldsymbol{r}_1)T^*(\boldsymbol{r}_3,\boldsymbol{r}_4)T^*(\boldsymbol{r}_{2'},\boldsymbol{r}_{1'})T(\boldsymbol{r}_{3'},\boldsymbol{r}_{4'})\rangle$ to focusing. Solid lines denote fields, while dashed lines denote their complex conjugates. The Hikami vertex H exchanges momenta at positions $\mathbf{H}$ in the medium, which are integrated over.

All phase factors in Eq. (21) cancel so that all N angular channels are correlated. We approximate $|G(2,S)|^2 \approx (\ell/4\pi)\delta_{2,S}$, which may have to be reconsidered for $R \approx S$ in the last line in Eq. (21) that will actually dominate. After some straightforward algebra, we find the lengthy expression for the half-space that consists of four terms,

$$B_2(\mathbf{r},\mathbf{r}_S) \equiv B_2^{(1)} + B_2^{(2)} + B_2^{(3)} + B_2^{(4)} = |\Phi_0|^2 N^2 N_H \frac{\ell^2}{(4\pi)^2}\int_0^\infty dz_1 e^{-z_1/\ell}\int_0^\infty dz_{1'} e^{-z_{1'}/\ell}\Big[-\frac{1}{2}\partial_{z_H} A(z_H=0,\mathbf{r},\mathbf{r}_S)\tilde{\mathcal{L}}(z_1,0)\tilde{L}(z_{1'},0)$$
$$+\frac{1}{2}\partial_{z_H}\big(\tilde{\mathcal{L}}(z_1,z_H=0)\tilde{\mathcal{L}}(z_{1'},z_H=0)\big)A(z_H=0,\mathbf{r},\mathbf{r}_S) + 2\int_0^\infty dz_H\,\partial_{z_H}\tilde{\mathcal{L}}(z_1,z_H)\partial_{z_H}\tilde{\mathcal{L}}(z_{1'},z_H)A(z_H,\mathbf{r},\mathbf{r}_S)$$
$$+\int d^3\mathbf{H}\big(-\nabla_c^2-\nabla_d^2\big)\tilde{\mathcal{L}}(z_1,z_H)\tilde{L}(z_{1'},z_H)\tilde{\mathcal{L}}(\mathbf{r}_c,\mathbf{r}_S)\mathcal{L}(\mathbf{r}_d,\mathbf{r})\Big], \tag{22}$$

where we have defined $\tilde{\mathcal{L}}(z,z') \equiv \mathcal{L}(z,z',\mathbf{q}=\mathbf{0})$, we defined z_H as the z-component of the location $\mathbf{H}$ of the Hikami box, and we introduced, for $R=(z,\boldsymbol{\rho})$,

$$A(z_H,\mathbf{r},\mathbf{r}_S) = \int d^2\boldsymbol{\rho}_H \mathcal{L}(z_H,z_S,\boldsymbol{\rho}_H)\mathcal{L}(z_H,z,\boldsymbol{\rho}_H-\boldsymbol{\rho})$$
$$= \int \frac{d^2\mathbf{q}}{(2\pi)^2}\mathcal{L}(z_H,z_S,\mathbf{q})\mathcal{L}(z_H,z,\mathbf{q})e^{-i\boldsymbol{q}\cdot\boldsymbol{\rho}},$$

which for $z_H \approx 0$ is proportional to the C_1 background in Eq. (15). We will dramatically simplify the lengthy expression (22) above. As was done before, we replace the integrals over the skin layer by $\ell f(0)$ when possible. In the first two terms of Eq. (22), the Hikami vertex is located near the sample surface. Their sum is proportional to $A(z_H=0,\mathbf{r},\mathbf{r}_S) - 2z_0\partial_{z_H}A(z_H=0,\mathbf{r},\mathbf{r}_S) \approx 0$, which vanishes since $A \sim (z_H+z_0)^2$ for $z_H < 0$. Hence $B_2^{(1)} + B_2^{(2)} = 0$ and the first two terms in Eq. (22) vanish.

In the third term $B_2^{(3)}$ of Eq. (22), the Hikami box is situated in the skin-layer $0 < z_H < \ell$ since the diffuse propagator in a half-space $\partial_{z_H}\tilde{\mathcal{L}}(1,z_H)$ vanishes for $z_H > z_1$. Therefore, it is proportional to $A(z_H=0,R,S)$ and constitutes as such a correction to the C_1 background derived in Eq. (15),

$$B_2^{(3)}(\mathbf{r}) = \frac{9|\Phi_0|^2N^2}{(k\ell)^2}\times 3\pi A(0,\mathbf{r},\mathbf{r}_S) = \frac{3\Omega_A}{4\pi}B_1(\mathbf{r}). \tag{23}$$

This confirms the angular coverage $\Omega_A/2\pi$ to be the leading parameter in our expansion of wave correlations. The background energy density $B_2^{(3)}(\mathbf{r})$ is, via the quantity $A(z_H,\mathbf{r},\mathbf{r}_S)$ that Fourier-transforms $\boldsymbol{q}$ to $\boldsymbol{\rho}$, the spatial equivalent of angular C_2 correlations outside the sample, discussed in Ref. [26].

The fourth term $B_2^{(4)}$ in Eq. (22) is known to be negligible in reflection or transmission correlations [20]; here, we find it is nonzero, hence it is a new feature due to the *internal source* invoked in this work. In this fourth term, the Hikami box H is located either *exactly* at the virtual source S or at the detection point R. The two diffusion operators generate $\delta(\boldsymbol{r}_H,\boldsymbol{r})\mathcal{L}(\mathbf{r}_H,\mathbf{r}_S) + \delta(\boldsymbol{r}_H,\boldsymbol{r}_S)\mathcal{L}(\mathbf{r}_H,\mathbf{r})$. This contribution $B_2^{(4)}$ can be interpreted as a diffuse propagation from the slab surface first to R and subsequently to S, or *vice versa*,

$$B_2^{(4)}(\mathbf{r}) = \frac{9|\Phi_0|^2N^2}{(k\ell)^2}\frac{3z_0^2}{2\ell}\times\left[\frac{1}{\sqrt{(z-z_S)^2+\rho^2}} - \frac{1}{\sqrt{(z+z_S+2z_0)^2+\rho^2}}\right]. \tag{24}$$

Equation (24) is singular when $R=S$, but a more detailed analysis (see Appendix B) shows that the singularity is an artifact of a previous approximation near the focal point S and that in reality the singular term smears out over one mean free path, thereby taking the finite value η/ℓ with $\eta = 1.3863$ for $R=S$. Since the C_1 peak is typically one wavelength in size, the C_2 density (24) can still be considered as a "background." Nevertheless, as soon as $R \approx S$ within a wavelength, an extra factor 2 shows up due to "Coherent Backscattering" of the waves released by the pointlike source above, and due to the so far neglected second term in Eq. (5). However, because the source is smeared out over a mean free path, its peak value is strongly suppressed, hence it is not discussed further.

C. Comparison of C_2 and C_1 contributions

Let us compare the magnitude of the background energy density B_2 produced by C_2 correlations to the density B_1 of the C_1 background found in Eq. (15), and calculate their ratio as a function of the depth z of point R, as summarized in Table I. The data in the table show that deep inside B_2 always dominates, as z_s/ℓ becomes sufficiently large to compensate for the small factor $3\Omega_A/(4\pi)$. Near the surface at $z=0$, the ratio B_2/B_1 is small and independent of z_S. Deep in the

TABLE I. Ratio of C_2 and C_1 contributions to the background energy density B_2 and B_1 on the axis $R = (z, \boldsymbol{\rho} = \mathbf{0})$ for several depths z (see Fig. 1). The first term, proportional to "1" in parentheses, is $B_2^{(3)}(z)/B_1(z)$, whose depth dependence cancels; the second term is $B_2^{(4)}/B_1(z)$ stemming from the new source around S, with $\eta = 1.38$. Both terms are of the same order at $z = 0$, but the second term rapidly dominates as the depth z increases. The ratio B_2/B_1 is a competition of the limited angular coverage of the array $\Omega_A/2\pi \ll 1$ and the large factor z_S/ℓ, especially near the focal point $S = (z_s, \boldsymbol{\rho} = \mathbf{0})$, due to the generated source.

Depth z	$B_2(z,0)/B_1(z,0)$
$z = 0$	$3\Omega_A/4\pi \times (1 + 2z_0/\ell)$
$z = z_S$	$3\Omega_A/4\pi \times \left(1 + 4\eta z_S^2/\ell^2\right)$
$z = \infty$	$3\Omega_A/4\pi \times (1 + 2z_S/\ell)$

medium, the focusing near S is dominated by B_2, and Eq. (17) must be replaced by the much larger ratio of background to focal peak, equal to

$$\frac{P_1}{B_1 + B_2} \approx \frac{P_1}{B_2} = \frac{2}{3\eta}(k\ell)^2. \tag{25}$$

The enhancement in Eq. (25) is substantially greater than 1 for the focusing to be efficient, but it no longer grows with depth z_s of the focal point and is also independent of the solid angle Ω_A.

Contrary to the background energy density B_1 of the C_1 correlations discussed in Sec. III A, Eq. (24) contains a genuine source of energy at the focal point S. The flux emitted by this source is given by $F_S = -D\int d^3\mathbf{r}\nabla^2 B_2^{(4)}(\mathbf{r})$, where the volume integral is taken around the point S (see Appendix A). Let us compare this flux to the total flux (19) leaving the sample, which is equal to

$$\frac{F_S}{F_1(z<0)} = \frac{\Omega_A}{\pi}, \tag{26}$$

that is, the relative source strength created by the wavefront-shaped signal in the medium depends only on the angular coverage of the array and is determined by Ω_A. The ratio is small due to the large C_1 source created at the incident surface.

D. C_3 and C_0 correlations

If we consider two Hikami crossings in the medium, a C_3 term appears that can correlate both input and output. More crossings involving four paths necessarily induce corrections to either C_2 or C_3, but no new class of correlations. A C_3 term to the energy density generates corrections that are proportional to $(\Omega_A/2\pi)^2$ that are thus negligible.

Because the focused energy is proportional to the LDOS [35], it is an interesting question what may happen in the case of focusing inside a 3D bandgap crystal, where the LDOS vanishes; see, for instance, Ref. [36], it is a relevant question how scatterers close to the focus affect the focusing profile, notably since the scatterers induce fluctuations in the LDOS. In Appendix C we discuss these so-called C_0 correlations. The conclusion is that these correlations contribute weakly to the peak profile with a relative weight $P_0/P_1 \sim 1/k\ell$ compared to the C_1 peak value in Eq. (11), which is of the order of up to 10^{-1}–10^{-2}, even in opaque samples made of ZnO or TiO_2 nanoparticles. The C_0 correlations do not contribute to the background, hence $B_0 = 0$.

IV. WAVEFRONT SHAPING TO FOCUS INSIDE A SLAB

In this section, we show that the considerations for a half-space in the previous sections change only quantitatively when the focusing is performed inside a slab of finite width L. The slab geometry is relevant as it allows us to investigate the relation between transmission and the focus; moreover, it is a common sample geometry in experiments [5,8].

In the C_1 approximation, the background energy density associated with C_1 is still given by Eq. (12), but it involves the diffuse propagator for a finite slab. Using radiative boundary conditions at both surfaces $z = -z_0$ and $z = L + z_0$, the propagator becomes

$$\mathcal{L}(z, z', \mathbf{q}) = \frac{12\pi}{\ell^3}\frac{\sinh q[L - \max(z,z') + z_0]\sinh q[\min(z,z') + z_0]}{q\sinh\left(q(L+2z_0)\right)}. \tag{27}$$

Hence, the background from Eq. (12) becomes

$$B_1(z, \boldsymbol{\rho}) = \frac{9|\Phi_0|^2N^2}{(k\ell^2)}\frac{z_0^2}{\Omega_A}\int d^2\mathbf{q}\, e^{i\mathbf{q}\cdot\boldsymbol{\rho}} \times \frac{\sinh q(L - z_S + z_0)\sinh q(L - z + z_0)}{\sinh^2\left(q(L+2z_0)\right)}, \tag{28}$$

which is valid for all $(z_S, L) \gg z_0$. With the expression for $\mathcal{L}(z, z', \boldsymbol{q})$ for the slab, the peak value from Eq. (11) for a half-space is modified for a slab to

$$P_1(\mathbf{r}_S, \mathbf{r}) = 9|\Phi_0|^2N^2P(\mathbf{r}_S, \mathbf{r})^2\frac{z_0^2}{\ell^2}\left(1 - \frac{z_S + z_0}{L + 2z_0}\right)^2, \tag{29}$$

which decreases smoothly with the depth z_S of the focus S. The enhancement defined as the ratio of the peak and the background can be written as

$$\frac{P_1(\mathbf{r} = \mathbf{r}_S)}{B_1(\mathbf{r} = \mathbf{r}_S)} = \frac{\Omega_A}{2\pi} \times [2k(z_s + z_0)]^2 \times R\left(\frac{z_s + z_0}{L + 2z_0}\right), \tag{30}$$

in terms of a function $R(x)$ with $R(0) = 1$ for the half-space, $R(1/2) = 0.361$ in the middle of a slab, and $R(1) = 0.139$ at the exit surface of a slab. The overall behavior is the same as in Eq. (17), namely that the energy enhancement greatly exceeds unity, being proportional to $(k\,z_S)^2\Omega_A \gg 1$. In other words, wavefront shaping to the exit surface of a slab is less favorable than to the middle of the slab. The same function R reduces the transverse width of the background energy density $\langle\rho^2\rangle_1$ around the focus S given by Eq. (16) for a half-space according to $\langle\rho^2(z=z_S)\rangle_1 \to \langle\rho^2\rangle_1 \times R[(z_s+z_0)/(L+2z_0)]$. Thus, the finite thickness of the slab reduces both the enhancement and the transverse size of the background.

The C_2 background density for the finite slab is given by Eq. (22), although with only an additional first term due to the transmitting surface $z_H = L$, which cancels for the same reason due to the radiative boundary condition. If we neglect all powers in (ℓ/L), we find that the third background term $B_2^{(3)}$ only contributes when the Hikami box resides in the skin layer, as for the half-space, so that the relation $B_2^{(3)}/B_1 = 3\Omega_A/4\pi$ for the half-space also applies to the slab. The last term of Eq. (22), involving the new source, becomes equal to

$$B_2^{(4)}(z,\boldsymbol{\rho}) = \frac{9|\Phi_0|^2N^2}{(k\ell)^2}\frac{3\pi z_0^2}{\ell}\Pi(z,z_S,\boldsymbol{\rho}) \times\left[\left(1-\frac{z+z_0}{L+2z_0}\right)^2+\left(1-\frac{z_S+z_0}{L+2z_0}\right)^2\right], \tag{31}$$

where $\Pi(z,z_S,\boldsymbol{\rho})$ is the energy density emitted by a diffuse point source at position $(z=z_S,\boldsymbol{\rho}=\mathbf{0})$ in the slab, which is given by

$$\Pi(z,z_S,\boldsymbol{\rho}) = \int \frac{d^2\mathbf{q}}{(2\pi)^2}e^{i\mathbf{q}\cdot\boldsymbol{\rho}}\frac{\sinh\left(q[L-\max(z,z_S)+z_0]\right)\sinh\left(q[\min(z,z_S)+z_0]\right)}{q\sinh\left(q(L+2z_0)\right)}. \tag{32}$$

Expression (32) diverges at the focal point S since an energy source is created that is in reality smeared out over a mean free path. The power emitted by this source is slightly less for a finite slab, and Eq. (26) for a semi-infinite medium is modified to

$$\frac{F_S}{F_1(z<0)} = \frac{\Omega_A}{\pi}\left(1-\frac{z_S+z_0}{2(L+2z_0)}\right). \tag{33}$$

This ratio slowly decreases to $\Omega_A/2\pi$ as the focal point S approaches the transmitting sample surface.

The varying background energy density in the slab leads to a nonzero transmission coefficient. Due to the wavefront-shaped incident beam, this transmission will not necessarily decay as the Ohmic law ℓ/L, as in the diffusion approximation. We assume the slab to be sufficiently optically thick such that $\ell/L \ll \Omega_A/\pi \ll 1$. The transmission induced by the C_1 correlations is proportional to $\ell/(L\Omega_A)$, so that C_2 contributions dominate. In particular, the source term $B_2^{(4)}$ given by Eq. (31) leads to a flux

$$\begin{aligned}F_2^{(4)}(z=L) &= -D\int d^2\boldsymbol{\rho}\,\partial_z B_2^{(4)}(z,\boldsymbol{\rho})\\ &= 9\frac{|\Phi_0|^2N^2}{(k\ell)^2}\pi z_0^2 v_E\left(\frac{z_S+z_0}{L+2z_0}\right)\left(1-\frac{z_S}{L+2z_0}\right)^2,\end{aligned} \tag{34}$$

where we neglect powers of (z_0/L'). For a finite slab thickness, the reflected current in Eq. (19) causes an extra factor $1 - z_S/(L+2z_0)$ due to the presence of $\mathcal{L}(0,z_S)$. The normalized transmission is thus equal to

$$T = \frac{\Omega_A}{2\pi}\frac{z_S+z_0}{L+2z_0}\left(1-\frac{z_S+z_0}{L+2z_0}\right) \leqslant \frac{\Omega_A}{8\pi}. \tag{35}$$

By focusing on a point in the slab, the transmission becomes finite, and it takes its largest value $T = \Omega_A/8\pi$ independent of thickness L when we focus on the middle of the slab. On the one hand, it is remarkable to find that wavefront shaping to a point causes the transmission—via the non-Gaussian C_2 correlations—to become *non-Ohmic*. Nevertheless, this notion is consistent with the known dominant role of C_2 correlations in WFS in transmission [16,21]. On the other hand, the maximum transmission differs markedly from the optimal transmission $T = 2/3$ established by random-matrix theory [16]. In contrast, in our *ab initio* wave formalism, the different transmission is due to the large C_1 reflection coefficient that stems from the traditional source created near the incident sample surface. The modes with optimized transmission somehow find a way to suppress this source.

We note that the energy density expressed by Eq. (31) is not mirror-symmetric with respect to the slab's center, not even for $z_S = L/2$. In contrast, the density associated with optimized transmission must be mirror-symmetric in the plane $z = L/2$, as explained in Sec. V below. Therefore, focusing on a point in the slab by wavefront shaping is not equivalent to optimizing the transmission, as previously surmised. This conclusion was previously already drawn by Zheng and Genack [11]. Here, we see that focusing on a point enhances the transmission significantly beyond the Ohmic expectation ℓ/L, which is explicitly attributed to the presence of an energy source at the focal point inside the random medium. The asymmetric energy density is clearly due to our choice to position the time-reversal array on the left, and not on the right; a mirror-symmetric energy density may be restored by using identical and independent arrays on *both* sides of the slab.

V. OPTIMIZED TRANSMISSION

In this section, we develop the idea that optimizing the transmission is related to the creation of an energy source inside the slab. We will show that different propositions for the energy density profile lead to strongly different profiles for the sources. Two general arguments are made.

The first argument concerns the spatial symmetry of the energy density. The procedure is first to optimize the WFS for each different realization to find perfect transmission, and next to average the associated energy density inside the slab over all realizations and with equal incident power. Having found a wavefront that gives perfect transmission ($T = 1$) for a given realization of the disorder in the slab, see Fig. 3 (left), the time-reversal operation reproduces the same process, see Fig. 3 (center), and yields again an optimal transmission ($T = 1$) with the same density profile. More precisely, this follows from the Stokes relation for the complex transmission

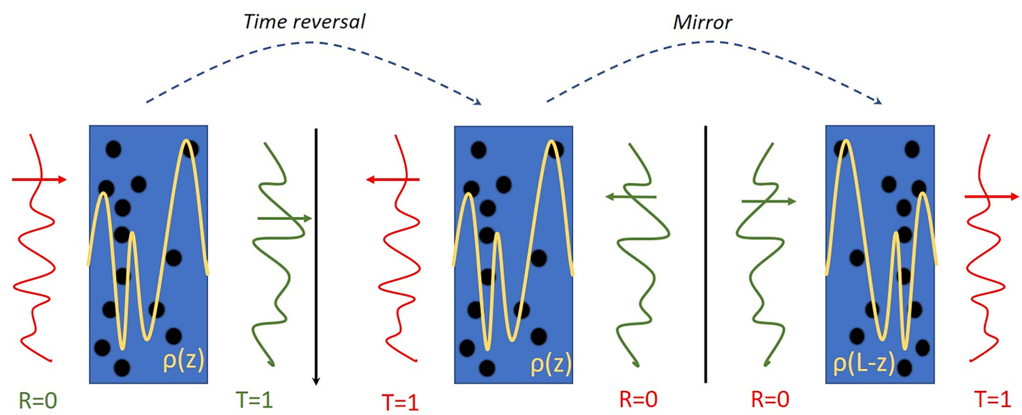

FIG. 3. Wavefront shaping and the energy density inside a slab. Left: if we optimize the total transmission, it is unity ($T = 1$), whereas total reflection vanishes ($R = 0$) and the energy density $\rho(z)$ varies wildly. Center: if we apply time reversal, the incident pattern (from left panel) is incident from the back surface without reflection ($R = 0$) and perfectly transmitted ($T = 1$) to the left entrance surface. The energy density $\rho(z)$ has the same pattern as it is not affected by time reversal. Right: if we apply a mirror operation, the incident wavefront from the center image is incident from the left, enters perfectly with ($R = 0$), and transmits perfectly ($T = 1$) to the right. The energy density $\rho(z)$ is mirrored with respect to left and center since the sample structure has been mirrored. Averaging over configurations yields a mirror-symmetric energy density, hence $\rho_M(z) = \rho_M(L - z)$.

matrix for the reversed process $\tilde{t}$ that obeys $\tilde{t}_{nm} = t_{mn}$. If we next perform a mirror operation of both the wave and the disorder, see Fig. 3 (right), we have constructed an incident wavefront that has the inverted energy density $\tilde{\rho}(x, y, z) = \rho(x, y, L - z)$ with respect to the initial process, yet still with perfect maximum transmission ($T = 1$). Assuming that we perform a perfect average over disorder, both energy densities will occur with the same statistical weight. The energy density ρ_M, averaged over disorder, *given* an optimal perfect transmission $T = 1$, must be *symmetric* about the central plane of the slab: $\rho_M(z) = \rho_M(L - z)$. Of course, this argument relies on the symmetry of the slab geometry and does not apply anymore when the sample geometry itself breaks mirror symmetry, as discussed by Koirala *et al.* [14].

The second argument, detailed in Appendix A, is that optimization to a point S in the medium produces an energy density whose average obeys a diffusion equation with the usual radiative boundary conditions at both sides, with same diffusion constant, and with some source related to the focal point proportional to the incident power. Even though we have seen above that optimizing to a focal point is not equivalent to optimizing the transmission, let us still speculate that the argument also applies for the optimized transmission, as confirmed by numerical simulations by Shi and Genack [37]. The energy density averaged over different optimizations of the transmission $\rho_M(z, \rho)$ must then be a superposition of the complete set of eigenfunctions of the diffusion equation with a source profile to be determined [12]. Let us ignore the complication of transverse energy profile, and integrate either over $\boldsymbol{\rho}$ or restrict to a quasi-1D geometry. The energy density would then be

$$\rho_M(z) = \frac{(L + 2z_0)s}{2\pi D} \sum_{n=1}^{\infty} \rho_M(n) \sin \frac{(2n - 1)\pi(z + z_0)}{L + 2z_0}, \quad (36)$$

which features only the *symmetric* modes with odd n, with a prefactor that depends on the source power S, including the total power s delivered by a hypothetical source, and with dimensionless coefficients $\rho_M(n)$ that determine the spatial density profile. For a *single* realization of the disorder, no rigorous relation exists between the density gradient and the transmission, hence optimization leads to zero reflection $R = 0$ and perfect transmission $T = 1$. After averaging, however, the diffusion picture emerges and the gradient of ρ_M at the boundaries determines the average outgoing flux, equal on both sides, hence $R = T$ and $R + T = 1$. The source power density $s(z)$ is then given by

$$s(z) = \frac{\pi s}{2(L + 2z_0)} \sum_{n=1}^{\infty} \rho_M(n)(2n - 1)^2 \times \sin \frac{(2n - 1)\pi(z + z_0)}{L + 2z_0}, \quad (37)$$

which is thus necessarily also symmetric around $z_S = L/2$. The extra factor $(2n - 1)^2$ implies the resurrection of high-order eigenfunctions in the Fourier expansion for the source that are not all positive-definite. Alternating signs with $\rho_M \sim (-1)^{n+1}$ generate more weight in the center, since for even n the eigenfunctions are all negative at the center of the sample.

In Table II we consider six different normalized sources. They all share a positive energy density *and* positive source density. The "flat" model was previously discussed by Davy *et al.* and corresponds to a homogeneous source density [13]. This model was generalized by Koirala *et al.* to the "best-fit" model, and the best fit to numerical simulation was obtained for $\alpha \approx 4 - \pi$ [14]. Furthermore, the simplest model "$n = 1$" keeps only the first eigenfunction, the only symmetric one that is positive-definite. Finally, the "symmetric normal incidence model" is associated with two equal sources close to both boundaries. This model clearly behaves differently from the

TABLE II. Properties of six different models for a 3D slab integrated over transverse dimensions $\boldsymbol{\rho}$ (alternatively: for a quasi-1D geometry). The total energy rate of all sources is normalized to S. We abbreviate $\tilde{z} \equiv (z+z_0)/(L+2z_0)$, $\tilde{z_0} = 2\ell/3(L+2z_0)$, and $G = 0.915\,965\ldots$ is Catalan's constant. The "best-fit" model with $\alpha = 4-\pi$ is a phenomenological model proposed by Ref. [14] with Fourier coefficients that decay relatively fast and as roughly $1/(2n-1)^{3.36}$. The symmetric plane-wave source corresponds to equal plane waves incident on both sides creating sources near both boundaries.

Model	Virtual source $[s/(L+2z_0)]$	Energy density $[(L+2z_0)s/D]$	$\rho_M(n)$	Energy $[(L+2z_0)^2 s/\pi^2 D]$	$\rho_M(L/2)/\rho_M(0)$ $[(L+2z_0)/\ell]$
Delta	$\delta(\tilde{z}-1/2)$	$\frac{1}{4}(1-\lvert 1-2\tilde{z}\rvert)$	$4(-1)^{n-1}/\pi(2n-1)^2$	1.234	0.750
Log-singular	$-\frac{\pi}{4G}\log\tan\frac{\pi}{2}\lvert\tilde{z}-\frac{1}{2}\rvert$	not ana	$(-1)^{n-1}/G(2n-1)^3$	1.080	0.548
$n=1$	$\frac{\pi}{2}\sin\pi\tilde{z}$	$\frac{1}{2\pi}\sin\pi\tilde{z}$	$\delta_{n,1}$	1.000	0.477
Best fit	$\frac{1-\alpha(3\tilde{z}^2-3\tilde{z}+1)}{[1-\alpha\tilde{z}(1-\tilde{z})]^3}$	$\frac{1}{2}\frac{\tilde{z}(1-\tilde{z})}{1-\alpha\tilde{z}(1-\tilde{z})}$	0.9966, −0.00295	0.996	0.295
($\alpha = 4-\pi$)			$+O(1)/(2n-1)^{3.36}$		
Flat ($\alpha = 0$)	1	$\frac{1}{2}\tilde{z}(1-\tilde{z})$	$8/[\pi^2(2n-1)^3]$	0.822	0.375
Symmetric	$L\delta(z)/2$	$\tilde{z}/2$ $(z<0)$	$\sin\pi(2n-1)\tilde{z_0}$	$\pi^2/2$	
normal	+	$\tilde{z_0}/2$ $(0<z<L)$	×	×	ℓ/L
incidence	$L\delta(L-z)/2$	$(1-\tilde{z})/2$ $(z>L)$	$4/\pi(2n-1)^2$	$\tilde{z_0}-\tilde{z_0}^2$	

others, because it decays slower with n, and the Fourier coefficients explicitly depend on ℓ/L. The physically reasonable conjecture of a positive-definite and mirror-symmetric source density filters out many solutions but clearly does not fix the profile. The total source power is normalized to s by imposing $\sum_{n=1}^{\infty}\rho_M(n)(2n-1) = 1$ so that $\rho_M(n)$ must decay at least as fast as $1/(2n-1)^3$. This explains partly why different models for the density profile in Table II have very similar shapes, especially when they are each normalized, as shown in Fig. 4(a). An extreme case, referred to as "Delta," has a point source at the center of the slab, yet it can clearly be rejected since its bilinear tentlike density differs markedly from numerical simulations that favor the "best-fit model" [see Fig. 4(a)]. In Fig. 4(b) we see that the source distributions vary strongly from one model to the other. The models "$n=1$" and "best fit" have rather similar sources but hardly distinguishable energy densities.

This discussion suggests that in order to discriminate between different models for optimized transmission, one should focus on the source density profile, rather than on the energy density. The "$n=1$" model seems to be an accurate candidate, but numerical simulations do reveal the significance of higher-n modes that represent 2% of the energy [12]. The "best-fit model" has a source density that deviates from the $n=1$ model near the boundaries, maybe because the diffusion approximation breaks down there. It is also remarkable that the very small value for $\rho_M(n=2)$ is 10× smaller than the one for the flat model. Finally, we are in a position to investigate the total energy in the slab associated with optimized transmission. Total energy for optimized transmission can be related to the average dwell time for the waves emitted by the source to reach the sample surface [38]. For $R=0$, $T=S=1$,

$$\int d^3\mathbf{r}\,\rho_M(\mathbf{r}) = \frac{d\phi_T}{d\omega} = \frac{(L+2z_0)^2}{\pi^2 D}\sum_{n=1}^{\infty}\frac{\rho_M(n)}{2n-1}. \quad (38)$$

The dwell time itself can be optimized [6] or manipulated [9] as well as the closely related delay time [2]. We infer from Table II that the stored energy varies only weakly among the different models for optimized transmission. This is due to the fact that the Fourier components in Eq. (38) decay as fast as $1/(2n-1)^4$. Because phase is measurable after optimizing transmission, this could be an opportunity to measure the diffusion coefficient in optimized transmission.

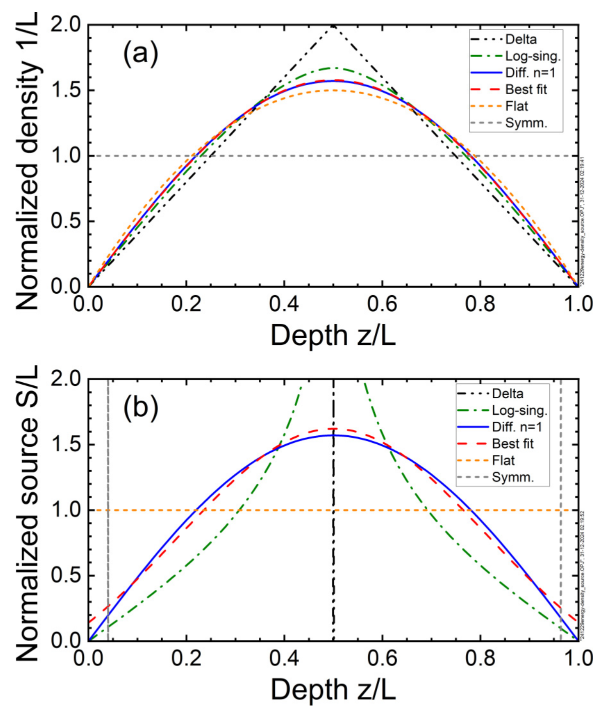

FIG. 4. (a) Normalized energy densities and (b) normalized sources for the six different models specified in Table II: Delta (black dash-double-dotted), log-singular (green dash-dotted), $n=1$ from diffusion (blue drawn), best fit (red dashed), flat (orange, short dashed), and symmetric (gray short dashed).

VI. CONCLUSION

In this work, we have applied mesoscopic speckle theory to describe the energy density created by a wavefront-shaped incident signal that focuses on a point in the random medium. The focus is determined by the short-range C_1 speckle, whereas the long-range C_2 speckle creates a background energy density that dominates deep inside the medium. This part also generates an energy source inside the medium. The focus is due to constructive interference between incoming and outgoing spherical waves, like in time-reversal experiments, and is not due to the source. We demonstrate the often implicit assumption that the background energy of the optimized profile, when averaged over different realizations and in experiments often performed over different frequencies, angles, channels, etc. [16], obeys a diffusion equation with the usual radiative boundary conditions. This settles one major challenge of this work. Because the C_1 speckle creates a source near the incident surface, much like an incident plane wave usually does in radiative transfer, the focusing to a point does not optimize transmission. We have developed the idea that optimizing transmission removes this C_1 source and creates a source for the diffuse energy background inside the sample associated with the optimized wavefront that is positive and mirror-symmetric. This argument leads to an energy density for which the lowest diffusion eigenmode dominates, as was shown first by Ojambati *et al.* [7] and later confirmed in more detail by Koirala *et al.* [14]. A major challenge exists to understand this profile from first principles and in particular why it is not exactly equal to the lowest mode.

ACKNOWLEDGMENTS

We thank Sergey Skipetrov for useful discussions. W.L.V. acknowledges the CNRS for a fellowship as a guest professor at the LPMMC, the LPMMC staff for their kind hospitality, the ESPCI for a fellowship as a guest professor at the Institut Langevin, and the Langevin staff for their kind hospitality. W.L.V. and A.L. acknowledge support by NWO-TTW Perspectief program P15-36 "Free-form scattering optics (FFSO)" in collaboration with TU Delft, TU Eindhoven, and industrial users ASML, Demcon, Lumileds, Schott, Signify, and TNO, as well by NWO-TTW Perspectief program P21-20 "Optical coherence; optimal delivery and positioning (OPTIC)" in collaboration with TU Delft, TU Eindhoven, ARCNL, and industrial users Anteryon, ASML, Demcon, JMO, Signify, and TNO.

APPENDIX A: CURRENT OF WAVEFRONT-SHAPED WAVES

1. Current of the background signal

The complex field sent back by the array after time reversal is given by Eq. (3). The background density was obtained in Eq. (12) in the C_1 approximation and in Eq. (22) in the C_2 approximation. They have in common that the last scatterer of field and complex conjugate before measurement is the same: $\mathbf{r}_4 = \mathbf{r}_4'$. The expressions for the background densities in both the C_1 and C_2 approximation can be summarized by the spatial correlation function

$$\langle \Phi(\mathbf{r})\Phi(\mathbf{r}')^* \rangle = \int d^3\mathbf{r}_4 f(\mathbf{r}_4) G(\mathbf{r}_4, \mathbf{r}) G^*(\mathbf{r}_4, \mathbf{r}'), \quad \text{(A1)}$$

with G the bulk Dyson Green's function given in Eq. (2), and $f(\mathbf{r})$ some real-valued function obtained from correlation functions that varies slowly on the scale of the mean free path. For monochromatic scalar waves, the cycled-averaged (radiative) density is proportional to $\rho(\mathbf{r}) = |\Phi(\mathbf{r})|^2$. For $\mathbf{r} = \mathbf{r}'$, we neglect spatial variation of $f(\mathbf{r})$ within a mean free path, and we use Eq. (7), giving

$$\langle \rho(\mathbf{r}) \rangle = \frac{\ell}{4\pi} f(\mathbf{r}). \quad \text{(A2)}$$

The cycle-averaged current-density is $\mathbf{J} = (c_0^2/\omega)\mathrm{Im}\, \Phi^*(\mathbf{r}) \boldsymbol{\nabla}\Phi(\mathbf{r})$. Using $\mathrm{Im}\, G^*(\mathbf{r})\boldsymbol{\nabla}G(\mathbf{r}) = k\hat{\mathbf{r}}|G(\mathbf{r})|^2$, we find from Eq. (A1), setting $\mathbf{x} = \mathbf{r} - \mathbf{r}_4$,

$$\begin{aligned}\langle \mathbf{J}(\mathbf{r}) \rangle &= \frac{kc_0^2}{\omega} \int d^3\mathbf{x} f(\mathbf{r} - \mathbf{x}) \hat{\mathbf{x}} |G(\mathbf{x})|^2 \\ &\approx \frac{kc_0^2}{\omega} \int d^3\mathbf{x} [-\boldsymbol{\nabla} f(\mathbf{r})] \mathbf{x}\hat{\mathbf{x}} |G(\mathbf{x})|^2 \\ &= -\frac{1}{3}\frac{c_0^2}{v_P} \ell \times \boldsymbol{\nabla}\langle \rho(\mathbf{r}) \rangle, \end{aligned} \quad \text{(A3)}$$

with v_P the phase velocity. This implies that the diffusion equation applies regardless of where $f(\mathbf{r})$ stems from, here from two-particle diagrams, and with the same diffusion coefficient as the one found for the one-particle Green's function (the matter energy density inside scatterers should be treated to find the correct velocity). Any source or sink of energy in the medium is characterized by a nonzero value for $\nabla^2\langle \rho(\mathbf{r}) \rangle$.

2. Source of focused signal

In this Appendix, we investigate the anisotropy of the focused energy around the focal point $\mathbf{r}_S$, and we determine the associated source. The average field at a point $\mathbf{r}$ near focal point S follows from Eq. (3),

$$\langle \Phi(\mathbf{r}) \rangle = N\Phi_0 \int_1 \int_2 e^{-z_1/\ell} \mathcal{L}(\mathbf{r}_1, \mathbf{r}_2) G(\mathbf{r}_S, \mathbf{r}_2) G^*(\mathbf{r}_2, \mathbf{r}). \quad \text{(A4)}$$

Let us recall that the factor Φ_0 has the same unit as the field unit, and that $|\Phi_0|^2$ has the dimension of field energy density. This expression contains a rapidly varying part on the scale of the wavelength, as well as an exponential decay of the Green's function $G(x)$ on the scale of the mean free path. Because $\mathcal{L}$ varies slower on this scale, we can substitute $\mathbf{x} = \mathbf{r} - \mathbf{r}_2$ and $\mathbf{y} = \mathbf{r} - \mathbf{r}_S$, and expand $\mathcal{L}(\mathbf{r}_1, \mathbf{r}_2)$ around $\mathbf{r}$ as

$$\int_2 \to \int d^3\mathbf{x} G(\mathbf{x} - \mathbf{y}) G^*(\mathbf{x}) [\mathcal{L}(\mathbf{r}_1, \mathbf{r}) - \mathbf{x} \cdot \boldsymbol{\nabla}_{\mathbf{r}} \mathcal{L}(\mathbf{r}_1, \mathbf{r})].$$

The integral over $\mathbf{r}_1$ generates $\ell\mathcal{L}(0, z, \mathbf{q} = \mathbf{0}) \equiv \ell\tilde{\mathcal{L}}(0, z)$. The integral over $\mathbf{x}$ can be performed to find

$$\langle \Phi(z, \mathbf{y}) \rangle \sim N\Phi_0 \ell^2 \left[P(y)\tilde{\mathcal{L}}(0, z) + \frac{i}{k} P'(y) \hat{\mathbf{y}} \cdot \nabla_z \tilde{\mathcal{L}}(z_1, z) \right],$$

with $P(y) = -\mathrm{Im}\, G(y)$. The second term in the expansion represents the anisotropic angular dependence of the focused field around the point S. The current density associated with this anisotropy is given by $\mathbf{J} = (c_0/k)\mathrm{Im}\langle\Phi^*\rangle\nabla_{\mathbf{r}}\langle\Phi\rangle$, involving the *average* field $\langle\Phi\rangle$. The released energy at distance y from the focal point follows from the energy flow $F(y)$ through a surface $A = 4\pi y^2$ around the source

$$F(y) = 4\pi y^2 \int d^2\hat{\mathbf{y}}\, \hat{\mathbf{y}} \cdot \mathbf{J}(\mathbf{r}_S, \mathbf{y}). \tag{A5}$$

The derivatives $\nabla_{\mathbf{y}}(\mathbf{y}P)$ cancel by parity in the angular integral. The derivative ∂_z in the current density $\boldsymbol{J}$ survives, and we obtain

$$F(y) = -\frac{N^2|\Phi_0|^2 c_0 \ell^4}{3k^2} y^2 P(y) P'(y) [\nabla_z \tilde{\mathcal{L}}(z=0, z=z_S)]^2. \tag{A6}$$

This current decays exponentially from the focal point S with the mean free path. Therefore, the focused signal is not associated with a net source.

APPENDIX B: PEAK VALUE FOR THE DIFFUSE C_2 SOURCE

The Hikami source derived in Eq. (22) is proportional to

$$I(\mathbf{r}, \mathbf{r}_S) = \int d^3\mathbf{r}_2 \int d^3\mathbf{r}_4 |G(\mathbf{r} - \mathbf{r}_2)|^2 \frac{1}{|\mathbf{r}_2 - \mathbf{r}_4|} |G(\mathbf{r}_S - \mathbf{r}_4)|^2, \tag{B1}$$

with $|G(\mathbf{x})|^2 = \exp(-x/\ell)/(4\pi x)^2$. For $\mathbf{r}_S$ and $\mathbf{r}$ separated by more than a mean free path ($|\mathbf{r}_S - \mathbf{r}| > \ell$), the two integrals decouple, and using Eq. (7), the Hikami source takes the form of a point source:

$$I(\mathbf{r}, \mathbf{r}_S) = \left(\frac{\ell}{4\pi}\right)^2 \frac{1}{|\mathbf{r}_S - \mathbf{r}|}. \tag{B2}$$

When $\mathbf{r}_S$ and $\mathbf{r}$ are closer, this is no longer valid. In the limit at which both positions coincide ($\mathbf{r}_S = \mathbf{r}$), we obtain

$$\begin{aligned} I(\mathbf{r}_S, \mathbf{r}_S) &= \frac{\ell}{(4\pi)^4} \int d^3\mathbf{x} \int d^3\mathbf{y} \frac{e^{-(x+y)}}{x^2 y^2} \frac{1}{|\mathbf{x} - \mathbf{y}|} \\ &= \frac{\ell}{(4\pi)^2} 2 \int_0^{\pi/4} \frac{d\phi}{\cos\phi(\cos\phi + \sin\phi)} \\ &= \left(\frac{\ell}{4\pi}\right)^2 \frac{1.3863}{\ell}. \end{aligned} \tag{B3}$$

This outcome corresponds to replacing $1/r$ in Eq. (B2) for $r = 0$ by η/ℓ, with $\eta = 1.3863$.

The power density of the source is equal to $\nabla \cdot \mathbf{J}$. The total power is proportional to

$$\int d^3\mathbf{r} (-\nabla^2) I(\mathbf{r}, \mathbf{r}_S) = 4\pi \left(\frac{\ell}{4\pi}\right)^2. \tag{B4}$$

This means that the point source in Eq. (B2) is in reality smeared out over one mean free path ℓ when $\mathbf{r}_S$ and $\mathbf{r}$ are near to each other, without affecting its total power.

APPENDIX C: C_0 CORRELATIONS

The C_0 correlation was first introduced by Shapiro as a fluctuation of the source power by a nearby scatterer, and it yields spatial correlations in the intensity of infinite range [22]. It was later shown that C_0 correlations are fluctuations of the local density of states, to which any source is sensitive [23–25]. Therefore, we consider here the importance of C_0 speckle for the quality of the focusing. We emphasize that even if the source S is virtual, the focusing at S is affected by nearby scatterers. The detection point R is assumed to contain no real detector, but fluctuations in LDOS at R do exist. The two C_0 diagrams contributing to this speckle are shown in Fig. 5. They describe the perturbation of both background and peak by a scatterer close to R and S. This implies immediately that both diagrams survive only when R and S are separated by at most one mean free path. Both diagrams thus contribute to the focusing and not to the background, and the infinite correlation of C_0 does not pertain to R. Let us first consider the right-hand-side figure. It correlates all incident channels, as was the case for the C_1 peak in Eq. (11). The calculation goes as before, leading to Eq. (11) with a minor modification of Eq. (7) that integrates out the positions $\mathbf{r}_2$ and $\mathbf{r}_{2'}$ near S. For scatterers "p" and scattering matrix t, this equation is replaced by

$$\begin{aligned} &\left(\frac{\ell}{4\pi}\right)^2 P(\mathbf{r}_S, \mathbf{r})^2 \\ &\quad \to 2 \times \int_{2,2'} \sum_p G(\mathbf{r}_2, \mathbf{r}_p) t G(\mathbf{r}_p, \mathbf{r}_S) G^*(\mathbf{r}_2, \mathbf{r}) \\ &\qquad \times G(\mathbf{r}_{2'}, \mathbf{r}) G^*(\mathbf{r}_{2'}, \mathbf{r}_p) t^* G^*(\mathbf{r}_p, \mathbf{r}_S) \\ &\quad = \left(\frac{\ell}{4\pi}\right)^2 \times \frac{8\pi}{\ell} \int d^3\mathbf{r}_p P(\mathbf{r}_p, \mathbf{r})^2 |G(\mathbf{r}_p, \mathbf{r}_S)|^2, \end{aligned} \tag{C1}$$

where we replace $\sum_p = \rho \int d^3\mathbf{r}_p$ and use $\rho|t|^2 = 4\pi/\ell$. The first factor in this equation is just the one found for the C_1 focusing peak, while the second factor stands for the relative C_0 correction. The integral over $\mathbf{r}_p$ averages out the oscillation of the sinc-function $P(\mathbf{r}_p, \mathbf{r})$, and this factor decays as $\exp(-|\mathbf{r}_{-}\mathbf{r}_S|/\ell)/k^2|\mathbf{r} - \mathbf{r}_S|^2$. For overlapping points $R = S$ we find the C_0 factor to be equal to $\pi/k\ell$, consistent with our previous work [23].

The diagram on the left of Fig. 5 can be treated similarly, but it suffers from decorrelation between the N channels, like the C_1 background in Eq. (12). This time the nearby scatterers p impose a factor different from the one in Eq. (C1), namely

$$\begin{aligned} \left(\frac{\ell}{4\pi}\right)^2 P(\mathbf{r}_S, \mathbf{r})^2 \to \mathrm{Re}\, \frac{8\pi}{\ell} \int d^3\mathbf{r}_p P(\mathbf{r}_p, \mathbf{r}) G^*(\mathbf{r}_p, \mathbf{r}) \\ \times P(\mathbf{r}_p, \mathbf{r}_S) G(\mathbf{r}_p, \mathbf{r}_S). \end{aligned} \tag{C2}$$

A detailed analysis shows that this expression decays exponentially with the distance between R and S as well, and thus contributes to the peak. For $S = R$ it takes again the value $\pi/k\ell$. However, this C_0 diagram is an extra factor $1/\Omega_A(kz_s)^2$ smaller than the one expressed by Eq. (C1) because this time the N elements are not all correlated. This C_0 diagram can thus safely be neglected.

We conclude that the C_0 correlations contribute to the focusing peak around the virtual source S with a relative weight $\pi/k\ell$. But the C_0 correlations do not significantly change the

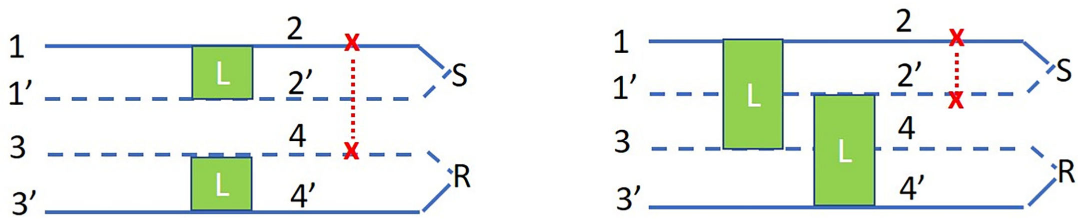

FIG. 5. C_0 contributions to the energy density at position R caused by a scatterer (in red) close to the focus locus S. Dashed lines denote complex-conjugate wave fields. Both actually generate a contribution to the peak, but only the left diagram suffers from decorrelation between the N channels. Complex conjugates of these diagrams exist but are not shown.

picture put forward by the C_1 approximation. Whereas the C_1 approximation typically predicts a diffraction-limited function $(\sin kx/kx)^2$, the C_0 peak decays as $\exp(-x/\ell)/(kx)^2$ around S with an amplitude that is smaller by a factor $\pi/k\ell$.

[1] A. P. Mosk, A. Lagendijk, G. Lerosey, and M. Fink, Controlling waves in space and time for imaging and focusing in complex media, Nat. Photon. **6**, 283 (2012).

[2] S. Rotter and S. Gigan, Light fields in complex media: mesoscopic scattering meets wave control, Rev. Mod. Phys. **89**, 015005 (2017).

[3] H. Cao, A. P. Mosk, and S. Rotter, Shaping the propagation of light in complex media, Nat. Phys. **18**, 994 (2022).

[4] S. Gigan, O. Katz, H. B. De Aguiar, E. R. Andresen, A. Aubry, J. Bertolotti, E. Bossy, D. Bouchet, J. Brake, S. Brasselet, Y. Bromberg, H. Cao, T. Chaigne, Z. Cheng, W. Choi, T. Cižmár, M. Cui, V. R. Curtis, H. Defienne, M. Hofer, R. Horisaki, N. C. Pégard *et al.*, Roadmap on wavefront shaping and deep imaging in complex media, J. Phys. Photon. **4**, 042501 (2022).

[5] I. M. Vellekoop and A. P. Mosk, Focusing coherent light through opaque strongly scattering media, Opt. Lett. **32**, 2309 (2007).

[6] M. Durand, S. M. Popoff, R. Carminati, and A. Goetschy, Optimizing light storage in scattering media with the dwell-time operator, Phys. Rev. Lett. **123**, 243901 (2019).

[7] O. S. Ojambati, H. Yilmaz, A. Lagendijk, A. P. Mosk, and W. L. Vos, Coupling of energy into the fundamental diffusion mode of a complex nanophotonic medium, New J. Phys. **18**, 043032 (2016).

[8] P. Hong, O. S. Ojambati, A. Lagendijk, A. P. Mosk, and W. L. Vos, Three-dimensional spatially resolved optical energy density enhanced by wavefront shaping, Optica **5**, 844 (2018).

[9] R. Sarma, A. G. Yamilov, S. Petrenko, Y. Bromberg, and H. Cao, Control of energy density inside a disordered medium by coupling to open or closed channels, Phys. Rev. Lett. **117**, 086803 (2016).

[10] N. Bender, A. Yamilov, A. Goetschy, H. Yilmaz, C. W. Hsu, and H. Cao, Depth-targeted energy delivery deep inside scattering media, Nat. Phys. **18**, 309 (2022).

[11] X. Cheng and A. Z. Genack, Focusing and energy deposition inside random media, Opt. Lett. **39**, 6324 (2014).

[12] O. S. Ojambati, A. P. Mosk, I. M. Vellekoop, A. Lagendijk, and W. L. Vos, Mapping the energy density of shaped waves in scattering media onto a complete set of diffusion modes, Opt. Express **24**, 18525 (2016).

[13] M. Davy, Z. Shi, J. Park, C. Tian, and A. Z. Genack, Universal structure of transmission eigenchannels inside opaque media, Nat. Commun. **6**, 6893 (2015).

[14] M. Koirala, R. Sarma, H. Cao, and A. Yamilov, Inverse design of perfectly transmitting eigenchannels in scattering media, Phys. Rev. B **96**, 054209 (2017).

[15] A. Derode, P. Roux, and M. Fink, Robust acoustic time reversal with high-order multiple scattering, Phys. Rev. Lett. **75**, 4206 (1995).

[16] I. M. Vellekoop and A. P. Mosk, Universal optimal transmission of light through disordered materials, Phys. Rev. Lett. **101**, 120601 (2008).

[17] B. A. van Tiggelen, Green function retrieval and time reversal in a disordered world, Phys. Rev. Lett. **91**, 243904 (2003).

[18] R. McIntosh, A. Goetschy, N. Bender, A. Yamilov, C. W. Hsu, H. Yilmaz, and H. Cao, Delivering broadband light deep inside diffusive media, Nat. Photon. **18**, 744 (2024).

[19] R. Berkovits and S. Feng, Correlations in coherent multiple scattering, Phys. Rep. **238**, 135 (1994).

[20] M. C. W. van Rossum and T. M. Nieuwenhuizen, Multiple scattering of classical waves: Microscopy, mesoscopy, and diffusion, Rev. Mod. Phys. **71**, 313 (1999).

[21] C. W. Hsu, S. F. Liew, A. L. Goetschy, H. Cao, and D. Stone, Correlation-enhanced control of wave focusing in disordered media, Nat. Phys. **13**, 497 (2017).

[22] B. Shapiro, New type of intensity correlation in random media, Phys. Rev. Lett. **83**, 4733 (1999).

[23] B. A. van Tiggelen and S. E. Skipetrov, Fluctuations of local density of states and C_0 speckle correlations are equal, Phys. Rev. E **73**, 045601(R) (2006).

[24] M. D. Birowosuto, S. E. Skipetrov, W. L. Vos, and A. P. Mosk, Observation of spatial fluctuations of the local density of states in random photonic media, Phys. Rev. Lett. **105**, 013904 (2010).

[25] V. Krachmalnicoff, E. Castanie, Y. De Wilde, and R. Carminati, Fluctuations of the local density of states probe localized surface plasmons on disordered metal films, Phys. Rev. Lett. **105**, 183901 (2010).

[26] L. Shaughnessy, R. E. McIntosh, A. Goetschy, C. W. Hsu, N. Bender, H. Yilmaz, A. Yamilov, and H. Cao, Multiregion light control in diffusive media via wavefront shaping, Phys. Rev. Lett. **133**, 146901 (2024).

[27] A. Ishimaru, *Wave Propagation and Scattering in Random Media* (Academic, New York, 1978), Vols. I and II.

[28] R. Carminati and J. C. Schotland, *Principles of Scattering and Transport of Light* (Cambridge University Press, UK, 2021).

[29] O. Akdemir, M. D. Truong, A. Rates, A. Lagendijk, and W. L. Vos, Probing the position-dependent optical energy fluence rate in three-dimensional scattering samples, Phys. Rev. A **110**, 033520 (2024).

[30] P. Blomgren, G. C. Papanicolaou, and H. Zhao, Super-resolution in time-reversal acoustics, J. Acoust. Soc. Am. **111**, 230 (2002).

[31] A. A. Chabanov, N. P. Tregoures, B. A. van Tiggelen, and A. Z. Genack, Mesoscopic correlation with polarization rotation of electromagnetic waves, Phys. Rev. Lett. **92**, 173901 (2004).

[32] S. Hikami, Anderson localization in a nonlinear-σ-model representation, Phys. Rev. B **24**, 2671 (1981).

[33] C. Draeger and M. Fink, One-time-reversal in chaotic cavities: Theoretical limits, J. Acoust. Soc. Am. **105**, 611 (1999).

[34] W. K. Hildebrand, A. Strybulevych, S. E. Skipetrov, B. A. van Tiggelen, and J. H. Page, Observation of infinite-range intensity correlations above, at, and below the mobility edges of the 3D Anderson localization transition, Phys. Rev. Lett. **112**, 073902 (2014).

[35] R. Sprik, B. A. van Tiggelen, and A. Lagendijk, Optical emission in periodic dielectrics, Europhys. Lett. **35**, 265 (1996).

[36] M. D. Leistikow, A. P. Mosk, E. Yeganegi, S. R. Huisman, A. Lagendijk, and W. L. Vos, Inhibited spontaneous emission of quantum dots observed in a 3D photonic band gap, Phys. Rev. Lett. **107**, 193903 (2011).

[37] Z. Shi and A. Z. Genack, Diffusion in translucent media, Nat. Commun. **9**, 1862 (2018).

[38] B. A. van Tiggelen, S. E. Skipetrov, and J. H. Page, Position-dependent radiative transfer as a tool for studying Anderson localization: Delay time, time-reversal and coherent backscattering, Eur. Phys. J. Spec. Top. **226**, 1457 (2017).